Applied Surface Science 566 (2021) 150607

Contents lists available at ScienceDirect

Applied Surface Science

journal homepage: www.elsevier.com/locate/apsusc

Full Length Article

# Kinetics of $HfO_2$ etching and impurity elimination with atomic hydrogen beams

Marcos Benedicto, Paloma Tejedor *

*Instituto de Ciencia de Materiales de Madrid, C.S.I.C.. Sor Juana Inés de la Cruz 3, 28049 Madrid, Spain*

ARTICLE INFO

*Keywords:*
$HfO_2$
Etch kinetics
Atomic H beams
Surface cleaning
ToF-SIMS
ARXPS

ABSTRACT

Modification of the surface composition, stoichiometry, morphology, and structure of $HfO_2$ ultra-thin layers upon exposure to atomic hydrogen beams has been investigated by a combination of time-of-flight secondary ion mass spectrometry (ToF-SIMS) depth profile analysis, angle-resolved x-ray photoelectron spectroscopy (ARXPS), atomic force microscopy (AFM) imaging, and transmission electron microscopy (TEM). The etching reaction has been found to be thermally activated ($E_a = 96$ kJ/mol) and governed by the expression $R_{etch}(Å/h) = 3.03 \times 10^8 e^{-\frac{1.15x10^4}{T}}$ within the 350–400 °C temperature range. The rate law determined experimentally, i.e., $R_{etch}(Å/h) = 1.07 \times 10^{-1}[H_2]^{1/2}$, is consistent with a reaction mechanism that involves the formation of a volatile hafnium dihydroxide, $Hf(OH)_2$ in two successive elementary steps. Precise control of the etching conditions allows to reach atomically smooth $HfO_2$ surfaces having r.m.s. roughness below 0.2 nm, with no evidence of Hf metal formation derived from the reaction with atomic H. Elimination of C, Cl, F, and S contaminants from the $HfO_2$ surface through the formation of the corresponding volatile hydrides has proved to be generally most effective at high temperatures and $H_2$ flow rates.

## 1. Introduction

Hafnium oxide ($HfO_2$) exhibits good mechanical, thermal and chemical stability at high temperatures, high refractive index ($n = 2.11$), wide bandgap (4.5–6.0 eV), high dielectric constant ($\kappa \simeq 16$–70), and high conduction band offset on Si (CBO $\simeq$ 1.5 eV) [1–4]. Due to these exceptional properties, $HfO_2$ has been deployed in the fabrication of energy-efficient windows [5], wear resistant and anti-reflection coatings [6,7], gas sensing devices [8], resistive random-access memory (RRAM) cells and field-effect transistors (FET) for ultra-scaled, high-density logic and memory applications [9–14]. In ultimately scaled FET devices the integration of the high-κ gate dielectric $HfO_2$ with a III-V compound semiconductor having higher mobility than silicon will be needed [15]. Given that most of these high mobility III-V semiconductors, e.g., InAs, InGaAs, have high dielectric constants and hence inferior electrostatic integrity, it will be also necessary the use of an ultrathin body (UTB) channel-on-insulator structure in a multigate configuration to reduce short channel effects (SCE) and enhance the device drive current [16,17]. Direct wafer bonding [18–21] and epitaxial lateral overgrowth (ELO) [22–24] of the III-V compound on the $HfO_2$ ultrathin gate are the main approaches reported to date to form the UTB channel-on-insulator structure. Sulfur passivation [19], thermal $InAsO_x$ interfacial layers [18] and low energy electron cyclotron resonance plasma [25] treatments are some of the strategies described in the literature to achieve a high quality III-V/high-κ interface by direct wafer bonding. In the ELO approach, in turn, III-V epitaxial growth has to be carried out in high or ultra-high vacuum on an atomically smooth and impurity-free $HfO_2$ surface in order to achieve an abrupt, oxide- and defect-free III-V/high- κ interface. Therefore, having an in-situ process that adequately prepares the surface of the $HfO_2$ prior to epitaxial growth would be most desirable.

Hydrogen has been profusely investigated in microelectronics as a means to remove native oxides from semiconductor surfaces [26–27], to induce the passivation and volatility of defects [28–29] and to modify epitaxial growth kinetics [30,31]. Studies on the effect of $H_2$ annealing on the properties of $HfO_2$ have shown that high temperatures can lead to oxygen deficiency in the dielectric and increased surface roughness during crystallization of the monoclinic phase [32]. Furthermore, high-pressure $H_2$ annealing of $HfO_2/Al_2O_3$/InGaAs MOS capacitors has proven effective at passivating interface states, although degradation of the leakage current and out-diffusion of In and Ga into the high-κ dielectric gate stack were also observed [33]. Kaviani *et al.* [34] used

* Corresponding author at: Universidad Pontificia Comillas ICAI-ICADE, Alberto Aguilera 23, 28015 Madrid, Spain.
*E-mail addresses:* mbcordoba@icai.comillas.edu (M. Benedicto), ptejedor@icmm.csic.es (P. Tejedor).

https://doi.org/10.1016/j.apsusc.2021.150607
Received 13 November 2020; Received in revised form 28 May 2021; Accepted 8 July 2021
Available online 18 July 2021

density functional theory calculations to examine the interaction of hydrogen with amorphous a-$HfO_2$ as a possible origin of the charge instability observed in CMOS devices when the hafnia film thickness decreased to the range of a few nanometers. Their results revealed that charged states of hydrogen in $HfO_2$ were thermodynamically more stable than the neutral state at all Fermi level positions, particularly the charged state that results from the donation of an electron to trapping sites, i.e., oxygen vacancies, grain boundaries, accompanied by the formation of O-H bonds at $HfO_2$ lattice sites.

While the thermodynamics and the effects on materials and device properties have been previously investigated, a kinetic study of the interaction of hydrogen with $HfO_2$ has not yet been addressed, despite its interest for the development of epitaxial UTB channel-on-insulator devices. The present paper is devoted to elucidating the kinetics and mechanism of the surface modification undergone by a-$HfO_2$ upon exposure to atomic H beams under ultra-high vacuum conditions and low temperatures. Based on ToF-SIMS profile analysis, we show that under the conditions examined an etching reaction that follows half-order kinetics takes place at the $HfO_2$ surface. A reaction pathway in which the rate limiting step is the formation of an adsorbed $Hf(OH)_2$ intermediate is then proposed to account for the experimentally observed rate law. Finally, we discuss the effect of the etching conditions on the $HfO_2$ surface morphology, structure, and the concentration of the most relevant impurities.

## 2. Material and methods

$HfO_2$ layers with a nominal thickness between 12 and 14 nm were deposited in an electron-beam evaporation system (Oerlikon Leybold Vacuum, Lab 600) on (0 0 1)-oriented n-type GaAs wafers with a rate of 0.1 Å/s at a substrate temperature of 150 °C under $O_2$ at a total pressure of $7.5 \times 10^{-5}$ Torr. The as-deposited $1 \times 1$ $cm^2$ $HfO_2$/GaAs samples were mounted onto 5 cm diameter molybdenum platens and introduced in the growth chamber of a solid-source III-V molecular beam epitaxy system (RIBER Compact-12 MBE), operating at a base pressure of $1 \times 10^{-10}$ Torr and equipped with a home-built hydrogen thermal cracker cell. The cracker cell consists of a tungsten capillary heated by electron bombardment from a tungsten filament located at its front end, where the dissociation of the effusing hydrogen beam takes place. An acceleration voltage of 2.5 kV was applied from a home-built power supply to obtain ionization currents in the 30–35 mA range and filament temperatures around 1800 °C. The supply of $H_2$ gas (Praxair, $\geq$ 99.9999% purity) to the cracker cell was varied between 0.1 and 0.4 sccm by means of a mass flow controller (M200 MKS). The $HfO_2$/GaAs samples were first outgassed at 350 °C during 45 min and then exposed to the dissociated atomic H beam at substrate temperatures between 350 and 400 °C for 30 min at a background pressure of $1–2 \times 10^{-6}$ Torr. Under these conditions the estimated atomic H flux on the sample is $1.2–6.0 \times 10^{16}$ H atoms/s. As H atoms impinge on the $HfO_2$ sample at rather high temperatures, diffusion over the surface and saturation coverage with chemisorbed hydrogen is favored [35–37]. After exposure to the atomic H beam the samples were cooled down to room temperature at a rate of 4 °C/min and covered with a few monolayers-thick As capping layer to protect the surface against atmospheric contamination prior to elemental analysis by ToF-SIMS.

Mass spectra, elemental maps and depth profiles of the $HfO_2$ samples exposed to the atomic H beam were acquired in dual-beam mode, using a ToF-SIMS IV instrument (ION-TOF GmbH, Germany) equipped with a 1 keV $Cs^+$ ion sputter gun and a 25 keV $Bi_3^+$ liquid metal ion gun (LMIG) used as the primary ion source for analysis, mounted at an angle of 45° with respect to the sample surface. The secondary ions generated by bombardment with the pulsed $Bi_3^+$ beam were extracted with a 10 kV voltage and their time of flight from the sample to the detector were measured by means of a reflectron mass spectrometer. The area for analysis was 126x126 $\mu m^2$ with a pixel resolution of 256x256 and the ion fluence was kept below the static limit ($1 \times 10^{12}$ ions/$cm^2$). A low-energy electron flood gun was applied for charge compensation during all depth profiles analysis. Negative secondary ions mass spectra were acquired in the mass range of $0 < m/z < 1000$. Negative polarity was chosen due to the much higher secondary ion yield of oxide matrices with respect to metal ones. We obtained moderately high mass resolution (m/Δm) values of the secondary ion peaks in the negative spectra, which varied between 3000 and 9000. Negative spectra were calibrated using the $H^-$, $C^-$, $CH^-$, $C_2^-$, $C_3^-$, $C_3H^-$, $C_4^-$, $C_4H^-$, $C_5^-$, $C_5H^-$, $C_6^-$, $C_6H^-$ peaks before further analysis of the samples was carried out. The ions represented in the depth profiles included in this work are those shown in Table. 1:

Angle-resolved x-ray photoelectron spectroscopy (ARXPS) was used to analyze the stoichiometry of the $HfO_2$ layers deposited on the GaAs substrates after exposure to atomic H. These studies were carried out using a Thermo Scientific Theta Probe spectrometer equipped with a Double-Focusing Full 180° spherical sector analyzer and monochromatic Al radiation with a spot size of $400 \times 400$ $\mu m^2$. The excitation source energy was 1486.6 eV. The angle resolution needed for monitoring compositional depth profiles was achieved by varying the detector-sample between 24.88° and 81.13°. All signals were calibrated with respect to the position of C 1s, located at 285 eV. The surface morphology of the samples treated with atomic H was examined by AFM using a Nanotec Electrónica commercial instrument working in dynamic mode. Etched single-crystalline silicon tips with a nominal end radius of 2 nm and resonance frequency 75 kHz were used with scans rates of 0.5 lines per second. The data were taken at 512 lines per scan. Finally, cross-sectional $HfO_2$/GaAs specimens were examined in a Philips Tecnai 20 TEM/STEM operating at 200 keV and equipped with a field emission gun (FEG) and an integrated system for Energy Dispersive X-ray Spectroscopy (EDS) and Electron Energy Loss Spectroscopy (EELS) analysis. Both bright field TEM images and high-angle annular dark field (HAADF) scanning TEM (STEM) images were recorded.

## 3. Results and discussion

### 3.1. $HfO_2$ etch kinetics

The etch kinetics of $HfO_2$ with hydrogen was investigated by examining the variation of the etch rate with substrate temperature and $H_2$ flow rate for a constant exposure to the atomic H beam of 30 min. The results are gathered in Figs. 1 and 2. Etch depths were determined from ToF-SIMS depth profiles by measuring the sputtering time employed to reach the $HfO_2$/GaAs interface, taking into account the sputtering rate calibrated by optical profilometry in the 126x126 $\mu m^2$ analysis crater for each sample. Fig. 1(a) shows the ToF-SIMS depth profiles corresponding to $HfO_2$/GaAs samples exposed to the atomic H beam generated by dissociation of 0.1 sccm $H_2$ at substrate temperatures between 350 °C and 400 °C, where a clear increase in etch depth with temperature can be observed. Likewise, ToF-SIMS depth profiles of $HfO_2$ samples exposed to atomic H for the same length of time at a constant temperature of 400 °C showed an increase in etch depth with $H_2$ flow rate, as depicted in Fig. 1(b). Under the experimental conditions studied the calculated etch rates varied between 2.7 Å/h and 13.0 Å/h (0.5–2.5 ML/h), which allows for a precise layer-by-layer control of the $HfO_2$ etching reaction with atomic hydrogen.

The Arrhenius plot depicted in Fig. 2(a) confirmed that the etching reaction is thermally activated and governed by the expression $R_{etch}$(Å/h) $= 3.03 \times 10^8\ e^{-\frac{1.15x10^4}{T}}$, from which an associated activation energy of

**Table 1**
List of negative ions whose ToF-SIMS depth profiles are studied in this work.

| Center Mass (u) | 210.91 | 143.83 | 1.01 | 12.00 | 19.00 | 34.97 | 31.97 |
|---|---|---|---|---|---|---|---|
| Ion Assignment | $^{179}HfO_2^-$ | $GaAs^-$ | $H^-$ | $C^-$ | $F^-$ | $Cl^-$ | $S^-$ |

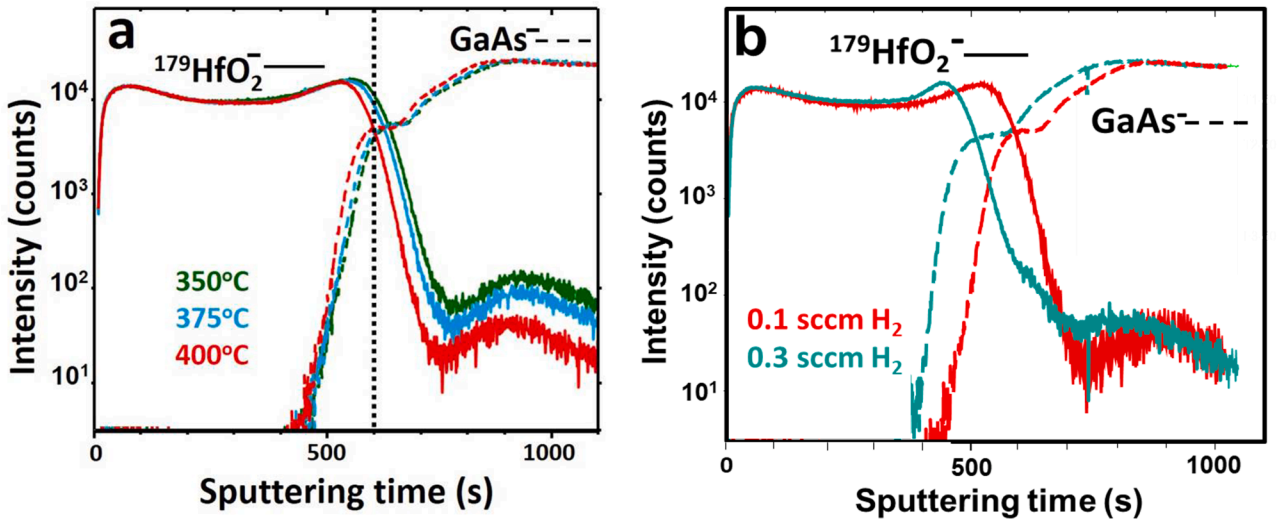


**Fig. 1.** ToF-SIMS depth profiles of the $^{179}HfO_2^-$ and $GaAs^-$ ions (a) after exposure to an atomic H beam at substrates temperatures between 350 °C and 400 °C using a constant $H_2$ flow rate of 0.1 sccm, (b) after exposure to atomic H showing the effect of the $H_2$ flow rate on the etch depth at a constant substrate temperature of 400 °C (As-deposited $HfO_2$ layer thickness: 12 nm). As an example, we show in (a) a vertical dotted line indicating the position of the $HfO_2$/GaAs interface used to calculate the etch depth in the sample treated with atomic H at 400 °C.

96 kJ/mol has been calculated. The reaction order with respect to $H_2$ was then determined from the etch rate dependence on $H_2$ flow rate in a series of $HfO_2$/GaAs samples treated with atomic H, using flow rates between 0.1 and 0.4 sccm at a constant substrate temperature of 370 °C. As shown in Fig. 2(b), the reaction order derived from the slope of the log–log plot of the etch rate vs. the $H_2$ flow rate was found to be ½. In consequence, the experimental rate law derived from the graph has the expression $R_{etch}(Å/h) = 1.07 \times 10^{-1}[H_2]^{1/2}$.

Once the rate law was determined experimentally, we proceeded to postulate a reaction pathway consistent with the observed etch kinetics. Numerous investigations have demonstrated that the reaction of metal oxides with high temperature hydrogen or water vapors leads to material loss through the formation of volatile hydroxides or oxyhydroxides [38–42]. In these works, identification of the volatile species was carried out by using the transpiration technique, Knudsen effusion mass spectrometry, free jet expansion mass spectrometry and kinetic studies based on the dependence of the hydroxide species flux on partial pressure of the gaseous reactant (i.e. reaction order). In the absence of thermochemical data relative to hafnium hydroxides and oxyhydroxides at elevated temperatures, we considered in our analysis hafnium di- and tetra hydroxides as possible products of the etch reaction with atomic H, given that their existence had been previously verified by means of Fourier-transform infrared (FTIR) spectroscopy and confirmed by electronic structure calculations [43]. In order to discriminate between these two hydroxide species, we evaluated the two alternative reaction pathways by comparing the expression of the rate equation derived for each case. While the resulting rate equation pointed to a reaction order n with respect to $H_2$ equal to 1 for the hypothesis of the $Hf(OH)_4$ product, we found a value of n = 1/2 for the formation of $Hf(OH)_2$ through two elemental reaction steps, the first being the rate limiting step of the overall reaction. In consequence, we consider that the most plausible mechanism of the interaction of atomic H with $HfO_2$ involves the following sequence of elementary reactions:

1 Dissociation of the $H_2$ molecule at the cracker cell:

$$H_2(g) \underset{k_{-1}}{\overset{k_1}{\rightleftarrows}} 2H(g) \tag{1}$$

2 Adsorption of atomic H radicals on terminal O atoms of the $HfO_2$ surface:

$$H(g) \underset{k_{-2}}{\overset{k_2}{\rightleftarrows}} H^*(ads) \tag{2}$$

3 Formation of adsorbed $Hf(OH)_2$* by reaction of atomic H with $HfO_2$ in two consecutive steps, the first of which is the rate-limiting step of the process:

$$HfO_2(s) + H^*(ads) \overset{k_3}{\rightarrow} Hf(OH)O^*(ads) \tag{3}$$

$$Hf(OH)O^*(s) + H^*(ads) \underset{k_{-4}}{\overset{k_4}{\rightleftarrows}} Hf(OH)_2{}^*(ads) \tag{4}$$

### 3.2. *Desorption of hafnium dihydroxide from the solid surface:*

$$Hf(OH)_2{}^*(ads) \underset{k_{-5}}{\overset{k_5}{\rightleftarrows}} Hf(OH)_2(g) \tag{5}$$

Considering that reactions (1) and (2) are sufficiently fast to reach equilibrium, their corresponding equilibrium constants K can be expressed as:

$$K_1 = \frac{k_1}{k_{-1}} = \frac{[H(g)]^2}{[H_2(g)]} \tag{6}$$

$$K_2 = \frac{k_2}{k_{-2}} = \frac{[H^*(ads)]}{[H(g)]} \tag{7}$$

The etching rate can be expressed as:

$$R_{etch} = k_3\,[HfO_2\,(s)]\,[H^*\,(ads)] = k_3'\,[H^*\,(ads)] \tag{8}$$

since the $HfO_2$ solid film is in excess with respect to the adsorbed H atoms, i.e. $[HfO_2(s)] \gg\gg [H^*\,(ads)]$, and its concentration can be assumed to be constant:

$$k_3' = k_3\,[HfO_2(s)] \tag{9}$$

Substituting equations (6) and (7) into (8) the etching rate can be expressed as a function of the $H_2$ gas concentration, i.e., flow rate, resulting in the following rate law:

$$R_{etch} = k_3'\,K_2\,K_1^{1/2}\,[H_2(g)]^{1/2} \tag{10}$$

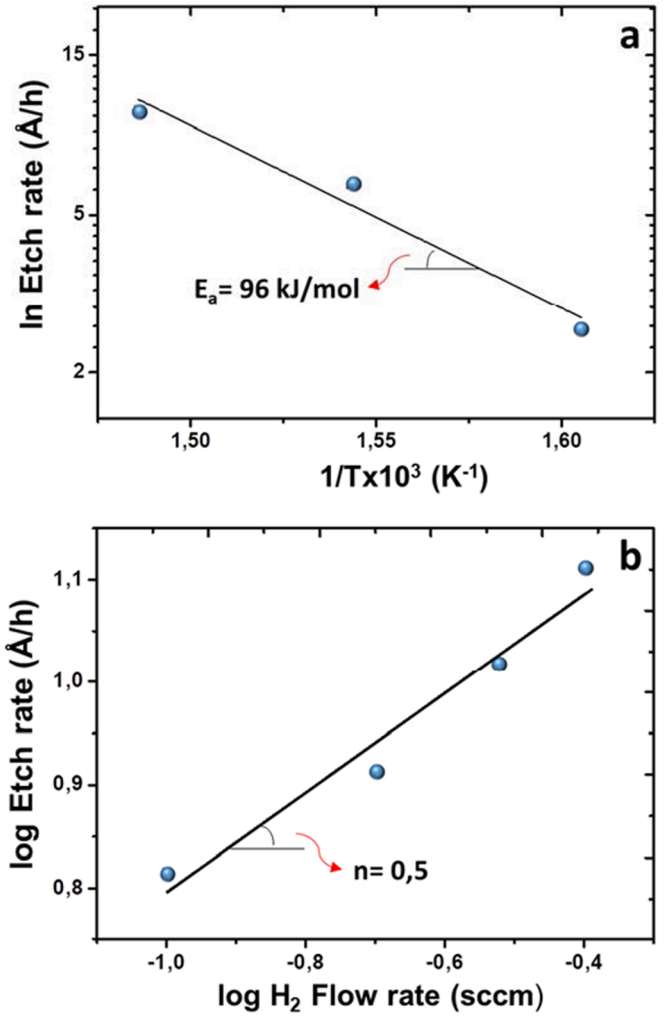


**Fig. 2.** Kinetics of the reaction of $HfO_2$ with atomic H: (a) Arrhenius plot for the 350–400 °C temperature range 400 °C and a constant $H_2$ flow rate of 0.1 sccm, showing an activation energy of 96 kJ/mol ($R^2 = 0.95$) and (b) Dependence of the $HfO_2$ etch rate on $H_2$ flow rate at a substrate temperature of 370 °C, rendering a reaction order of ½ with respect to $H_2$ ($R^2 = 0.95$).

which agrees with the etch rate dependence on $H_2$ flow rate determined experimentally, i.e., $R_{etch}(Å/h) = 1.07 \times 10^{-1}[H_2]^{1/2}$.

The reaction mechanism proposed here is supported by previous theoretical and experimental investigations on the interaction of group IV oxides with hydrogen and the formation of volatile hydroxides. As mentioned above, the formation of hafnium dihydroxide has been identified by infrared spectroscopy and confirmed by electronic structure calculations. In addition, density functional theory (DFT) calculations relative to the interaction of atomic H with a-$HfO_2$ have shown that the most favorable configuration is that where atomic H donates its electron to a trapping precursor state and the resulting proton forms a hydroxyl group bonded to a Hf atom [34,44]. The electron is predominately localized on two Hf ions, deforming the surrounding network due to weakening of the Hf-O bonds. This circumstance, together with the high kinetic energy of the impinging H atoms and the low pressure conditions used in the experiments, facilitates the desorption of the Hf $(OH)_2$ molecule from the surface.

### *3.3. Effect of atomic H on the composition, morphology and structure of the $HfO_2$ films*

ToF-SIMS depth profiles of atomic H in $HfO_2$/GaAs samples were investigated as a function of substrate temperature and $H_2$ flow rate. In general, we observed a maximum value of the H concentration at the oxide surface and a gradual decrease in the $HfO_2$ layer as the oxide/semiconductor interface was approached, indicating the existence of H diffusion towards the interior of the sample at the temperatures as low as 350 °C. Fig. 3 shows the depth profile of the $H^-$ ion in a sample after 30 min exposure to the atomic H beam at 400 °C using a $H_2$ flow rate of 0.1 sccm. It was also found that the H content in the $HfO_2$ layer decreased slightly with increasing temperature and $H_2$ flow rate, which is consistent with an increased fraction of H atoms being involved in the surface reaction with $HfO_2$ relative to those that diffuse into the layer as a consequence of the faster etch reaction kinetics.

The chemical composition in the near-surface region of the $HfO_2$ layers after exposure to atomic H in ultra-high vacuum was studied using ARXPS in parallel mode. The spectral features of the $HfO_2$ layers are presented in Fig. 4. Fig. 4(a) shows the ARXPS collapsed spectrum acquired with angles of 24° and 28° for a series of $HfO_2$/GaAs samples irradiated with atomic H at temperatures between 350 and 400 °C using $H_2$ flow rates in the 0.1–0.3 sccm range during 30 min. Two signals located at 18.5–19.5 eV and 17.0–17.5 eV, with a spin–orbit separation of 1.4 eV, were invariably observed. They are attributable to the $Hf^{4+}4f_{7/2}$ and $Hf^{4+}4f_{5/2}$ levels in $HfO_2$ (O-Hf-O-like bonds). The absence of signals at 14.4 eV and 15.4 eV, corresponding to $Hf^0$ $4f_{7/2}$ and $Hf^{x+}O_y$ $4f_{7/2}$ levels respectively [45,46], indicates that the $HfO_2$ film has not been reduced to metallic Hf or to a non-stoichiometric suboxide by reaction with atomic H. Therefore, under the experimental conditions deployed in this work the initial stoichiometry of the dielectric is preserved. In Fig. 4(b) we have gathered the high-resolution Hf4f and O1s ARXPS spectra for a $HfO_2$/GaAs sample irradiated at 400 °C with 0.1 sccm $H_2$ acquired at the surface and bulk (6 nm depth) with glancing angles of 81° and 25°, respectively. The low intensities registered for the surface spectra are due to the high glancing angle used in the measurements. As in Fig. 4(a), only the signals attributable to $HfO_2$ can be observed and therefore the formation of metallic Hf has to be ruled out.

The variation of the root mean square (r.m.s.) roughness of the $HfO_2$ film surface upon exposure to the atomic H beam for 30 min was studied by AFM as a function of substrate temperature and $H_2$ flow rate. The $HfO_2$/GaAs substrate temperature was varied between 350 and 400 °C, while the $H_2$ flow rate was controlled in the range 0.1–0.4 sccm. The effect of both variables on the film surface morphology can be seen in Fig. 5. Fig. 5(a) shows the increase in $HfO_2$ surface roughness with substrate temperature for a constant $H_2$ flow rate of 0.2 sccm, while the graph in Fig. 5(b) shows how the $HfO_2$ surface roughness decreases with

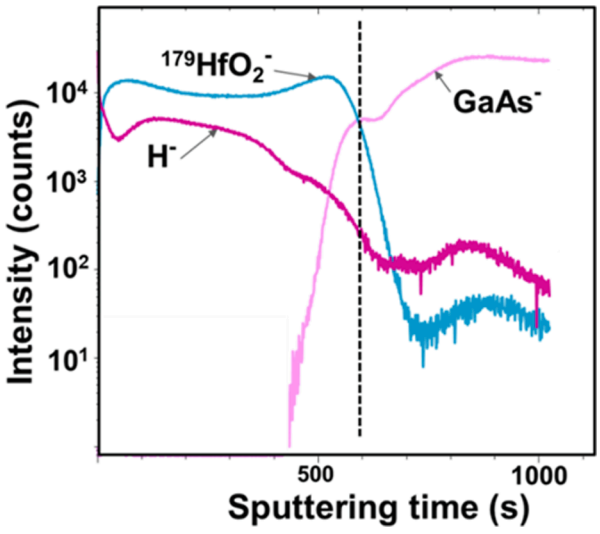


**Fig. 3.** ToF-SIMS depth profiles of the $H^-$, $^{179}HfO_2^-$, and $GaAs^-$ ions corresponding to a $HfO_2$/GaAs sample exposed to an atomic H beam at 400 °C for 30 min. $H_2$ gas flow rate: 0.1 sccm.

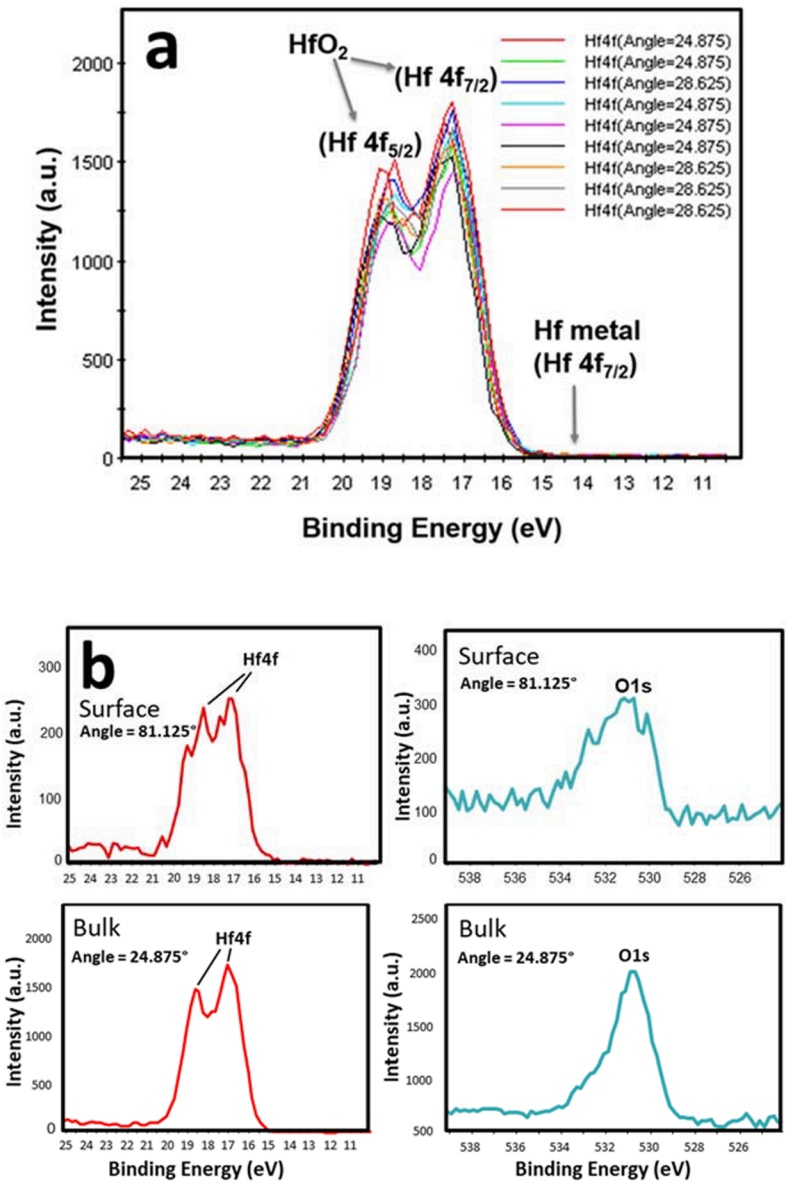


**Fig. 4.** (a) Collapsed ARXPS spectrum for a series of $HfO_2$/GaAs samples exposed to atomic H during 30 min in the 350–400 °C temperature range with 0.1–0.3 sccm $H_2$ flow rates, (b) High-resolution Hf4f and O1s ARXPS spectra of the surface and the bulk (6 nm depth) acquired with glancing angles of 81° and 25° for a $HfO_2$/GaAs sample irradiated at 400 °C with a 0.1 sccm $H_2$ flow rate.

increasing $H_2$ flow rate for a constant temperature of 370 °C.

The observed variations in morphology with temperature and reactant gas flow rate are characteristic of an etch process controlled by a surface chemical reaction. Migration of $O^{2-}$ and $Hf^{4+}$ ions are not likely to have a significant effect on the overall process, since they both exhibit a sub-diffusive behavior in amorphous $HfO_2$ arising from their nanoscale confinement, according to molecular dynamics simulations [47]. Despite the relatively low values of the diffusion coefficient of H in amorphous $HfO_2$ reported in the literature ($D_o = 7.2 \times 10^{10} cm^2/s$ at 255 °C) [48], the high temperatures and fluxes of the atomic H beam impinging on the $HfO_2$ thin film facilitate its diffusion over the surface, as mentioned above. The sticking coefficient of atomic H on $HfO_2$ decreases with increasing temperature and chemisorption takes place through formation of O-H bonds on active sites of the surface, where it is energetically most favored. According to *ab initio* calculations, once the strong O-H bonds have been formed on the surface, the hydroxyl groups are inmobile [49]. The etching reaction thus occurs at preferential locations on the surface, leading subsequently to an inhomogeneous desorption of the reaction products. The result of this anisotropic etching is the increase in $HfO_2$ surface roughness observed experimentally. By contrast, larger $H_2$ flow rates lead to higher H coverages of the $HfO_2$ surface and, as a consequence, desorption of the reaction products occurs to a greater extent and more homogeneously over the surface. Under these conditions, the etching rate is not sensitive to specific sites or directions on the surface due to a uniform removal rate of surface atoms, i.e., isotropic etching, which leads to a much smoother etching morphology [50]. The 1 μm × 1 μm AFM images inserted in the graphs illustrate these differences. Those samples exposed to low atomic H fluxes at high temperatures exhibit an irregular morphology with protrusions where chemisorption was less favorable. In contrast, samples treated with higher atomic H fluxes ($H_2$ flow rates $\geq$ 0.35 sccm) and relatively low temperatures ($\leq$375 °C) lead to an atomically flat surface (rms $\leq$ 0.2 nm), characteristic of a highly homogeneous layer-by-layer chemical etch process.

Fig. 6(a) depicts the cross-sectional TEM image of a $HfO_2$/GaAs sample after irradiation with atomic hydrogen at 400 °C with a 0.3 sccm $H_2$ flow rate. The surface roughness derived from the etching process and the onset of $HfO_2$ crystallization reported by other authors [51] can

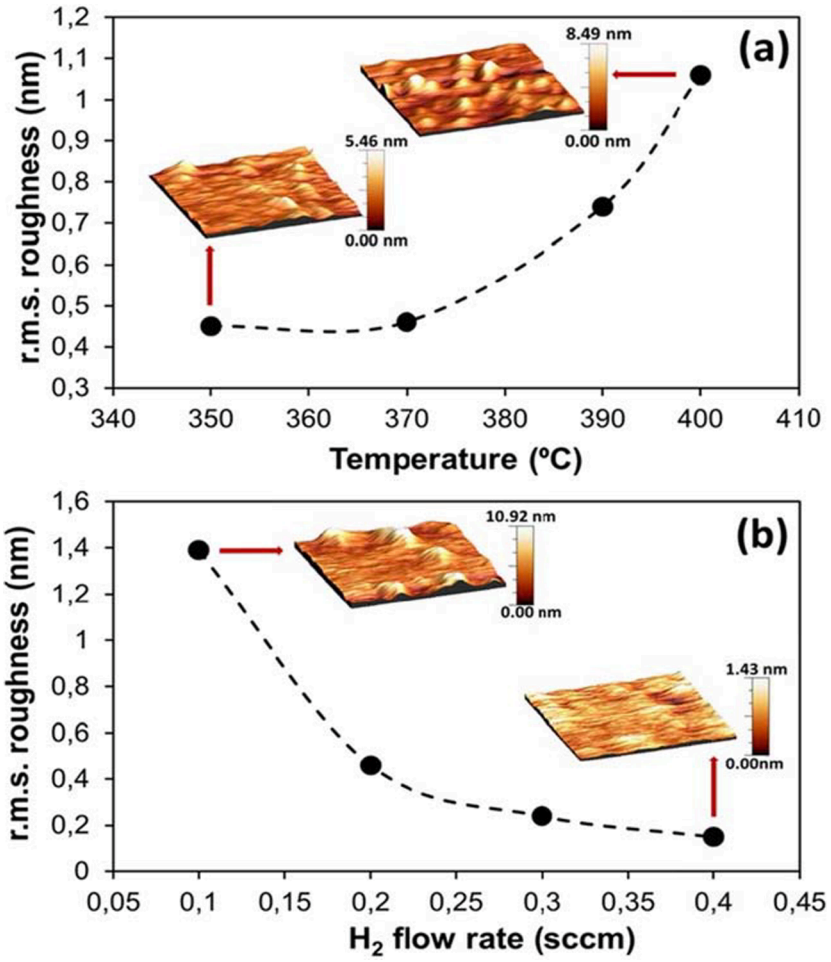


**Fig. 5.** Variation of the $HfO_2$ surface roughness with (a) substrate temperature for a constant $H_2$ flow rate of 0.2 sccm and with (b) $H_2$ flux rate for a substrate temperature of 370 °C. Insets are 1 μm × 1 μm AFM images of the surface topography corresponding to the experimental data pointed by the red arrows.

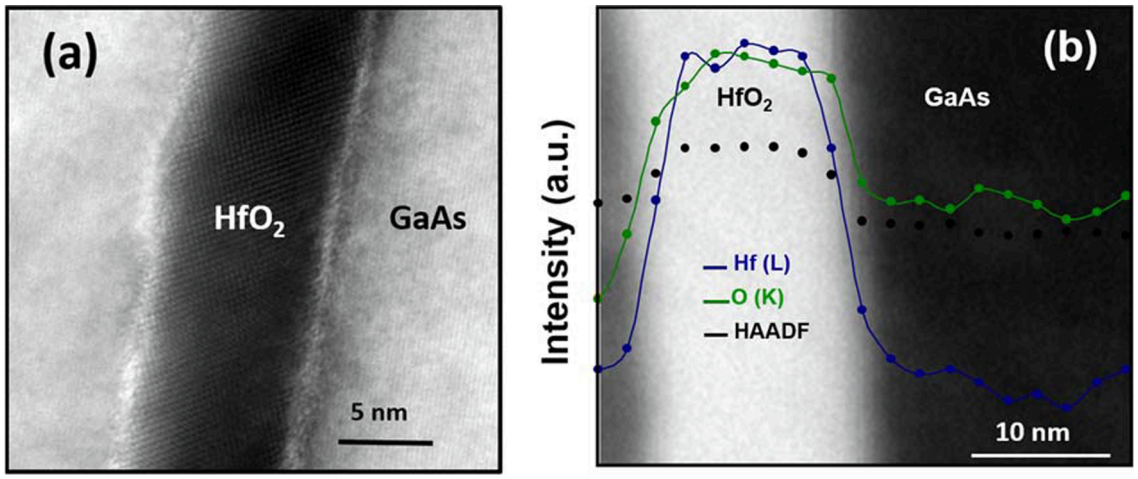


**Fig. 6.** (a) Cross-sectional TEM micrograph of a $HfO_2$/GaAs sample after irradiation with atomic H for 30 min at 400 °C with a 0.3 sccm $H_2$ flow rate and (b) STEM image, HAADF intensity profile, EDS scan profile of Hf (L) and EELS scan profile of O (K) for a sample irradiated at 400 °C with a 0.1 sccm $H_2$ flow rate.

be observed in this image. In Fig. 6(b) we show the STEM image and HAADF intensity profile, together with the EDS scan profile of Hf (L) and EELS scan profile of O (K), where the cross-sectional composition of the $HfO_2$ layer was investigated in a sample irradiated with atomic H at 400 °C with a 0.1 sccm $H_2$ flow rate. As shown in the image, the Hf and HAADF signals track each other, thus facilitating the identification of the $HfO_2$ layer. The elemental profiles indicate that neither Hf nor O diffuse appreciably into the GaAs substrate at the temperature of the experiment and within the resolution of the EDS scans (2 nm), no distinct interlayer is observable between the $HfO_2$ layer and the GaAs substrate. Furthermore, the relative profile heights of Hf and O signal do not evidence the formation of a metallic Hf layer on the surface resulting from

the reduction of $HfO_2$ with atomic H.

### 3.4. Effect of atomic H on $HfO_2$ impurity content

Carbon, chlorine, fluorine, and, to a lesser extent, sulphur were the main impurities found in the $HfO_2$ thin films during ToF-SIMS analysis. Their content variation upon irradiation of the $HfO_2$/GaAs samples with atomic H for 30 min was investigated as a function of substrate temperature and $H_2$ flow rate. Fig. 7 gathers the ToF-SIMS depth profiles corresponding to C, Cl, F, and S after exposure to the atomic H beam at temperatures between 350 °C and 400 °C using a constant $H_2$ flow rate of 0.1 sccm. The graphs illustrate the diffusion behavior and the reduction in concentration with increasing substrate temperature undergone by all the impurities analyzed. Out-diffusion of impurities from the $HfO_2$/GaAs interface most certainly occurs due to temperature gradients during $HfO_2$ thin film deposition and later during exposure to the atomic H beam. In the latter case, diffusion also occurs as a result of the concentration gradient created in the thin film as the impurities are being removed from the surface by atomic H through the formation of volatile hydrides. Regarding the effect of $H_2$ flow rate on the concentration profiles of these impurities in the $HfO_2$ film, we have found that, with the exception of F, their concentration also decreased when the flow rate was raised from 0.1 sccm to 0.3 sccm, as depicted in Fig. 8.

The differences in behavior observed in the graphs depend on the origin of the impurity and its interaction with atomic H. The depth profiles suggest that C contamination comes from the $HfO_2$ surface, the most probable sources being the organic solvents used to clean the $HfO_2$ sample, atmospheric $CO_x$ and traces of hydrocarbons present in the $H_2$ gas source or the vacuum system. Part of the C accumulated on the surface reacts with the impinging H flux, while another fraction diffuses into the oxide during processing. The surface reaction proceeds more rapidly at higher temperatures, reducing the available population of C atoms that diffuse into the $HfO_2$ layer, as seen in Fig. 7. On the other hand, the fact that the concentration of C in the $HfO_2$ bulk is reduced when the flow rate of $H_2$ is increased to 0.3 sccm, while the concentration on the surface increases, suggests that at high flow rates the arrival date of unintentional C contamination coming from the impinging H beam is faster than the etching rate of pre-deposited C on the surface. Similarly, due to its presence as trace impurity in $H_2$, the F concentration present in both bulk and surface of the $HfO_2$ layer increases with $H_2$ flow rate, as shown in Fig. 8.

Contamination of the $HfO_2$/GaAs interface with Cl and S, on the other hand, stems from dipping the sample in a HCl solution to remove native oxides from the GaAs surface and its subsequent passivation with $(NH_4)_2S$ prior to $HfO_2$ deposition. Both impurities out-diffuse during processing towards the oxide surface, where they react with the impinging H atoms. As illustrated by the depth profiles shown in Fig. 8, the concentration of both elements diminishes when the $H_2$ flow rate is increased, thus indicating that the surface reaction leading to their desorption is kinetically favored. Therefore, all the investigated impurities, with the exception of F, are more efficiently removed from the $HfO_2$ film at high substrate temperatures and high $H_2$ flow rates. This difference in behavior can be attributed to the fact that F is the only element more electronegative than O. As a consequence, F atoms present in $HfO_2$ bond to Hf dangling bonds, occupying O vacancies and reducing the trap density. For this reason, fluorine is considered as a good alternative to passivate the dielectric gate oxide and has been proposed to be intentionally incorporated to $HfO_2$ with the aim of improving its electrical properties [52,53].

The most likely mechanism responsible for the elimination of impurities from the $HfO_2$ surface is the formation of volatile hydrides [54–57], according to the following exothermic reactions:

$$C(ads) + 4H^*(ads) \leftrightarrows CH_4(g)\ \Delta H^0 = -75\ \text{kJ/mol} \quad (10)$$

$$Cl(ads) + H^*(ads) \leftrightarrows HCl(g)\ \Delta H^0 = -92\ \text{kJ/mol} \quad (11)$$

$$F(ads) + H^*(ads) \leftrightarrows HF(g)\ \Delta H^0 = -273\ \text{kJ/mol} \quad (12)$$

$$S(ads) + 2H^*(ads) \leftrightarrows H_2S(g)\ \Delta H^0 = -21\ \text{kJ/mol} \quad (13)$$

In order to gain a deeper understanding of the $HfO_2$ cleaning process we studied the temperature dependence of the surface impurity content. The Arrhenius plots in Fig. 9 depict the variation of the relative

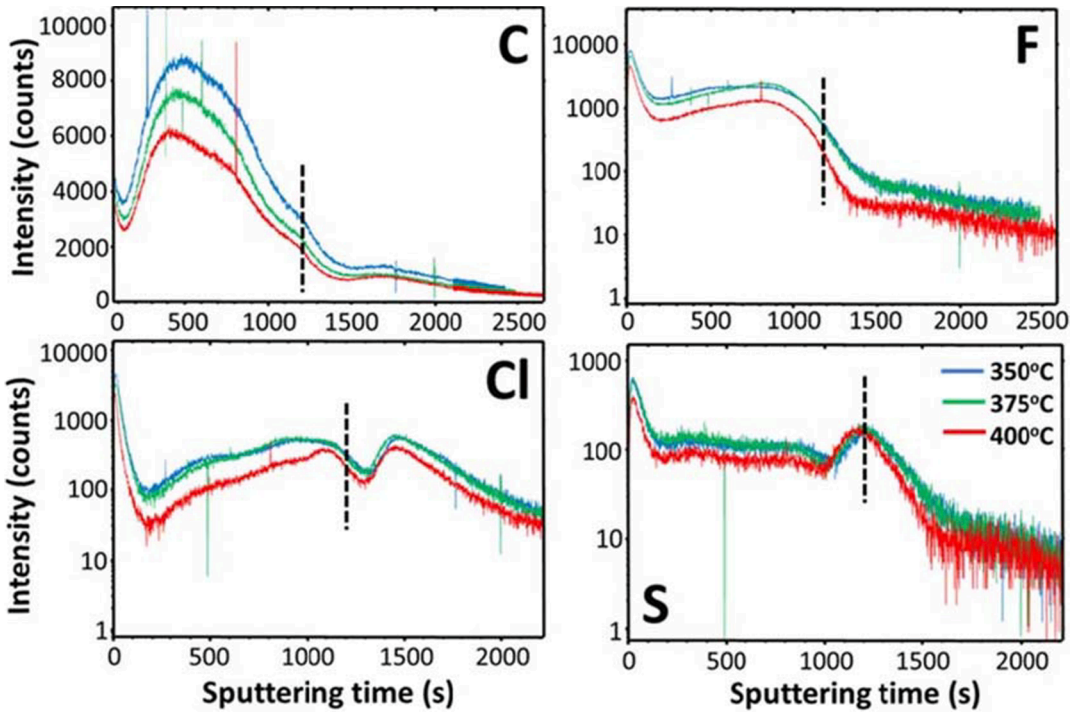


**Fig. 7.** Temperature dependence of the main impurities concentration profiles in $HfO_2$/GaAs samples irradiated during 30 min with atomic H using a constant $H_2$ flow rate of 0.1 sccm. The dotted lines indicate the position of the $HfO_2$/GaAs interface.

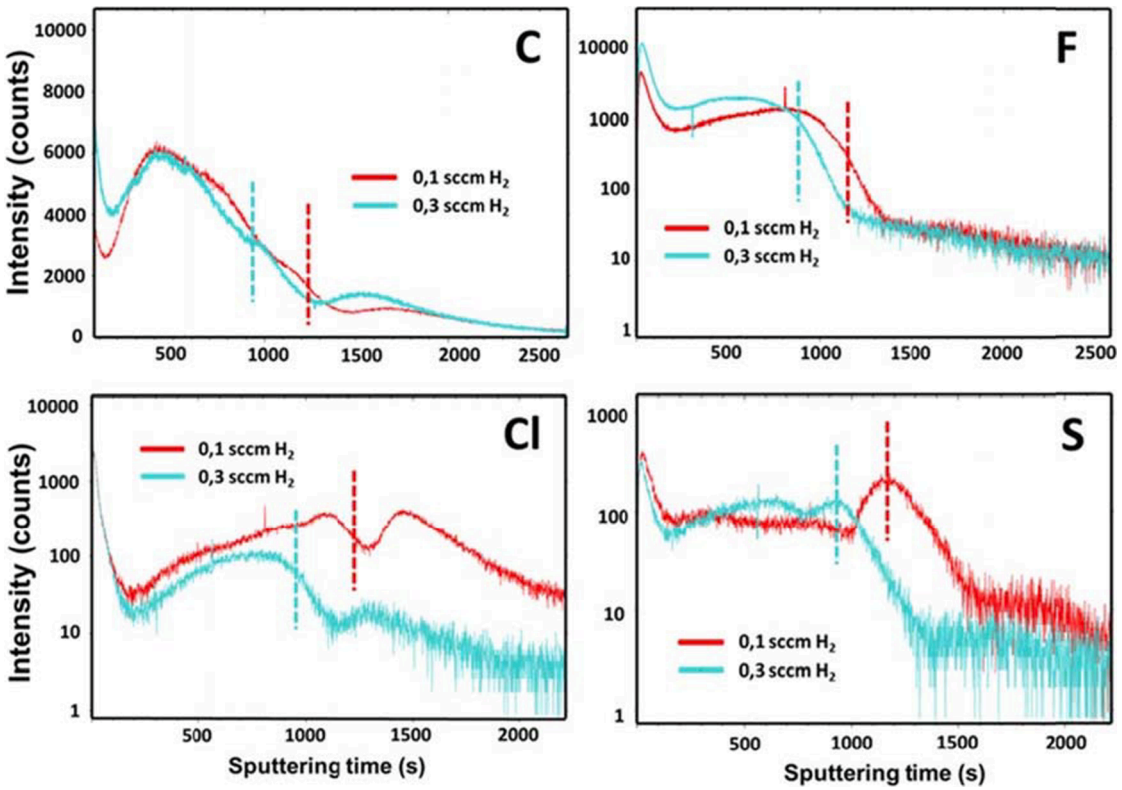


**Fig. 8.** Variation of the main impurities concentration profiles with $H_2$ flow rate in $HfO_2$/GaAs samples irradiated during 30 min with atomic H at a constant substrate temperature of 400 °C. The dotted lines indicate the position of the $HfO_2$/GaAs interface.

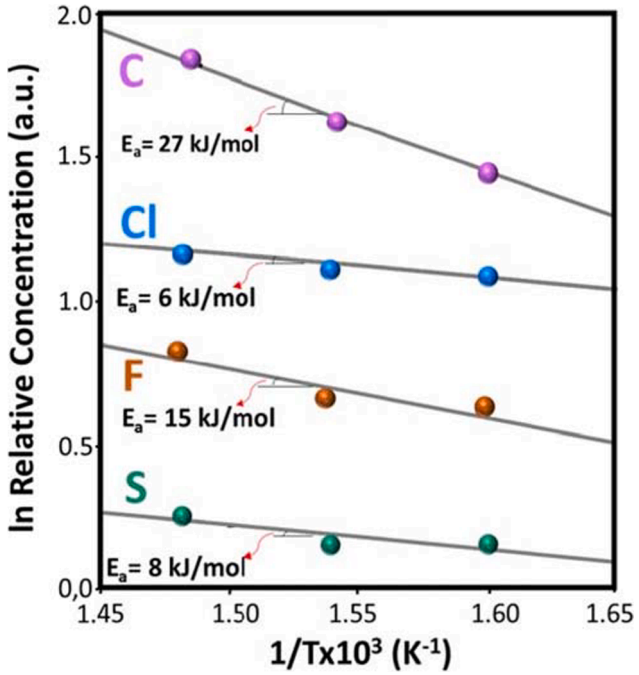


**Fig. 9.** Arrhenius plots showing the effect of substrate temperature on the relative concentration of C, Cl, F, and S at the $HfO_2$ surface (Sputtering depth = 0 nm), obtained from ToF-SIMS data for a constant 0.1 sccm $H_2$ flow rate.

concentration of C, Cl. F and, S at the $HfO_2$ surface with reciprocal temperature, confirming that their reaction with atomic H is thermally activated. The values of the activation energy derived from the graph range from 6 to 8 kJ/mol for weakly bound Cl and S to 27 kJ/mol for more strongly bound C, which point to the desorption of the corresponding hydride molecules, aided by the transfer of kinetic energy from the atomic H atoms [54], as the rate limiting step.

Finally, given that the $HfO_2$ etch morphology becomes rougher at high temperatures, a good compromise to obtain an atomically smooth (r.m.s. $< 0.2$ nm) $HfO_2$ surface with minimum impurity content that can be applied to form a high quality high-κ/III-V inverse interface is to carry out the etching experiments between 375 °C and 400 °C with a 0.3 sccm $H_2$ flow rate, as we have demonstrated for InGaAs channels deposited on nanopatterned $HfO_2$/GaAs by epitaxial lateral overgrowth [58].

## 4. Conclusion

We have studied the kinetics of the interaction of atomic hydrogen with the surface of $HfO_2$ in ultra-high vacuum as a function of temperature and flow rate of the $H_2$ feed gas. We have found that an etching reaction takes place at relatively low temperatures (350–400 °C), following half-order kinetics with respect to $H_2$ and having an associated activation energy of 96 kJ/mol. To account for the experimental rate equation, we have proposed a mechanism that includes the formation of an adsorbed $Hf(OH)_2$ species by direct reaction of atomic hydrogen radicals with the $HfO_2$ surface in two successive elementary steps, the first controlling the rate of the overall etching process. Due to this kinetic limitation, the etched thickness can be precisely controlled in the sub monolayer regime and the morphology adjusted to attain an atomically smooth $HfO_2$ surface. No secondary reaction leading to the reduction of $HfO_2$ to metallic Hf, nor significant changes in the crystallinity of the $HfO_2$ film occur in the temperature range examined. During the $HfO_2$ etching process with atomic hydrogen, the content of C, Cl, S, and F is reduced through the formation of volatile hydrides at the surface. The exothermic reactions leading to the formation of $CH_4$, HCl, $H_2S$, and HF are thermally activated and exhibit values of the activation energy (6–27 kJ/mol) that point to the desorption of the reaction products as the rate controlling step. Consequently, temperatures near

400 °C and $H_2$ flow rates above 0.3 sccm appear as the optimal conditions to achieve high quality $HfO_2$ surfaces for CMOS-compatible III-V/high-κ integration processes.

## Declaration of Competing Interest

The authors declare that they have no known competing financial interests or personal relationships that could have appeared to influence the work reported in this paper.

## Acknowledgments

We acknowledge support from Ministerio de Economía y Competitividad (Spain) under Grant no. TEC2016-78433 and CSIC Research Platform on Quantum Technologies PTI-001.

## References

[1] V. Dave, P. Dubey, H.O. Gupta, R. Chandra, Influence of sputtering pressure on the structural, optical and hydrophobic properties of sputtered deposited HfO2 coatings, Thin Solid Films 549 (2013) 2–7, https://doi.org/10.1016/j.tsf.2013.07.016.

[2] R. Chow, S. Falabella, M.R. Kozlowski, G.E. Loomis, F. Rainer, C.J. Stolz, Reactive evaporation of low-defect density hafnia, Appl. Opt. 32 (1993) 5567–5574, https://doi.org/10.1364/AO.32.005567.

[3] X. Zhao, D. Vanderbilt, First-principles study of structural, vibrational, and lattice dielectric properties of hafnium oxide, Phys. Rev. B 65 (2002), 233106, https://doi.org/10.1103/PhysRevB.65.233106.

[4] B. Johnson, J.L. Jones, Ferroelectricity in Doped Hafnium Oxide: Materials, Properties and Devices, in U. Schröder, C. S. Hwang, H. Funakubo (Eds.), Structures, Phase Equilibria, and Properties of HfO2, Elsevier B.V., 2019, pp. 25-45. https://doi.org/10.1016/B978-0-08-102430-0.00002-4.

[5] M.F. Al-Kuhaili, Optical properties of hafnium oxide thin films and their application in energy-efficient windows, Opt. Mater. 27 (2004) 383–387, https://doi.org/10.1016/j.optmat.2004.04.014.

[6] M. Gilo, N. Croitoru, Study of HfO2 films prepared by ion-assisted deposition using a gridless end-hall ion source, Thin Solid Films 350 (1999) 203–208, https://doi.org/10.1016/S0040-6090(99)00226-6.

[7] Y. Wang, Z. Lin, X. Cheng, H. Xiao, F. Zhang, S. Zou, Study of HfO2 thin films prepared by electron beam evaporation, Appl. Surf. Sci. 228 (2004) 93–99, https://doi.org/10.1016/j.apsusc.2003.12.028.

[8] C.H. Chang, K.W. Lin, H.H. Lu, R.C. Liu, W.C. Liu, Hydrogen sensing performance of a Pd/HfO2/GaOx/GaN based metal-oxide-semiconductor type Schottky diode, Int. J. Hydrogen Energy 43 (2018) 19816–19824, https://doi.org/10.1016/j.ijhydene.2018.08.213.

[9] L. Goux, P. Czarnecki, Y.Y. Chen, L. Pantisano, X.P. Wang, R. Degraeve, B. Govoreanu, M. Jurczak, D.J. Wouters, L. Altimime, Evidences of oxygen-mediated resistive-switching mechanism in TiN\HfO2\PtTiN\HfO2\Pt cells, Appl. Phys. Lett. 97 (2010), 243509, https://doi.org/10.1063/1.3527086.

[10] J. Müller, T.S. Böscke, U. Schröder, R. Hoffmann, T. Mikolajick, L. Frey, Nanosecond polarization switching and long retention in a novel MFIS-FET based on ferroelectric HfO2, IEEE Electron. Device Lett. 33 (2012) 185–187, https://doi.org/10.1109/LED.2011.2177435.

[11] T. Mikolajick, S. Slesazeck, M.H. Park, M.H. Schroeder, Ferroelectric hafnium oxide for ferroelectric random-access memories and ferroelectric field-effect transistors, MRS Bull. 43 (2018) 340–346, https://doi.org/10.1557/mrs.2018.92.

[12] F. Ali, D. Zhou, M. Ali, H.W. Ali, M. Daaim, S. Khan, M.M. Hussain, N. Sun, Recent progress on energy-related applications of HfO2-based ferroelectric and antiferroelectric materials, ACS Appl. Electron. Mater. 2 (2020) 2301–2317, https://doi.org/10.1021/acsaelm.0c00304.

[13] K. Mistry, C. Allen, C. Auth, B. Beattie, D. Bergstrom, M. Bost, M. Brazier, M. Buehler, et al., A 45 nm logic technology with high-k+metal gate transistors, strained silicon, 9 Cu interconnect layers, 193nm dry patterning, and 100% pb-free packaging, technical digest - international electron devices meeting, IEDM (2007) 247–250, https://doi.org/10.1109/IEDM.2007.4418914.

[14] A. Veloso, T. Huynh-Bao, P. Matagne, D. Jang, G. Eneman, N. Horiguchi, J. Ryckaert, Nanowire & nanosheet FETs for ultra-scaled, high-density logic and memory applications, Solid-State Electron. 168 (2020), 107736, https://doi.org/10.1016/j.sse.2019.107736.

[15] J.A. del Alamo, Nanometre-scale electronics with III–V compound semiconductors, Nature 479 (2011) 317–323, https://doi.org/10.1038/nature10677.

[16] S.H. Park, Y. Liu, N. Kharche, M. Salmani-Jelodar, G. Klimeck, M.S. Lundstrom, M. Luisier, Performance comparisons of III-V and strained-Si in planar FETs and nonplanar FinFETs at Ultrashort Gate Length (12nm), IEEE Trans. Electron Devices 59 (2012) 865, https://doi.org/10.1109/TED.2012.2198481.

[17] V.P. Popov, V.A. Antonov, A.K. Gutakovskiy, I.E. Tyschenko, V.I. Vdovin, A. V. Miakonkikh, K.V. Rudenkod, Hafnia and alumina stacks as UTBOXs in silicon-on insulator, Solid-State Electron. 168 (2020), 107734, https://doi.org/10.1016/j.sse.2019.107734.

[18] H. Ko, K. Takei, R. Kapadia, S. Chuang, H. Fang, P.W. Leu, K. Ganapathi, E. Plis, H. S. Kim, S.-Y. Chen, M. Madsen, A.C. Ford, Y.-L. Chueh, S. Krishna, S. Salahuddin, A. Javey, Ultrathin compound semiconductor on insulator layers for high-performance nanoscale transistors, Nature 468 (2010) 286–289, https://doi.org/10.1038/nature09541.

[19] M. Yokoyama, T. Yasuda, H. Takagi, N. Miyata, Y. Urabe, H. Ishii, H. Yamada, N. Fukuhara, M. Hata, M. Sugiyama, Y. Nakano, M. Takenaka, S. Takagi, III-Vsemiconductor-on-insulator n-channel metal-insulator-semiconductor field-effect transistors with buried Al2O3 layers and sulfur passivation: Reduction in carrier scattering at the bottom interface, Appl. Phys. Lett. 96 (2010), 142106, https://doi.org/10.1063/1.3374447.

[20] L. Czornomaz, N. Daix, D. Caimi, M Sousa, R. Erni, M. D. Rossell, M. El-Kazzi, C. Rossel, C. Marchiori, E. Uccelli, M. Richter et al., An integration path for gate-first UTB III-Von-insulator MOSFETs with silicon, using direct wafer bonding and donor wafer recycling, Technical Digest - International Electron Devices Meeting, IEDM 2012, 23.4.1-23.4.4. doi: 10.1109/IEDM.2012.6479088.

[21] J.-P. Shim, S.K. Kim, H. Kim, G. Ju, H. Lim, S.H. Kim, H.-J. Kim, Double-gated ultra-thin-body GaAs-on-insulator p-FETs on Si, APL Mater. 6 (2018), 016103, https://doi.org/10.1063/1.5000532.

[22] M. Shichijo, R. Nakane, S. Sugahara, S. Takagi, Fabrication of III–V on insulator structures on Si using microchannel epitaxy with a two-step growth technique, Jpn. J. Appl. Phys. 46 (2007) 5930–5934, https://doi.org/10.1143/JJAP.46.5930.

[23] C. Convertino, C. Zota, H. Schmid, D. Caimi, M. Sousa, K. Moselund, L. Czornomaz, InGaAs FinFETs directly integrated on silicon by selective growth in oxide cavities, Materials 12 (2019) 87, https://doi.org/10.3390/ma12010087.

[24] C. Zhang, X. Miao, K.D. Chabak, X. Li, A review of III–V planar nanowire arrays: selective lateral VLS epitaxy and 3D transistors, J. Phys. D: Appl. Phys. 50 (2017), 393001, https://doi.org/10.1088/1361-6463/aa7e42.

[25] M. Yokoyama, R. Iida, Y. Ikku, S. Kim, H. Takagi, T. Yasuda, H. Yamada, O. Ichikawa, N. Fukuhara, M. Hata, M. Takenaka, S. Takagi, Formation of III–V-on-insulator structures on Si by direct wafer bonding, Semicond. Sci. Technol. 28 (2013), 094009, https://doi.org/10.1088/0268-1242/28/9/094009.

[26] C. Auth et al., A 22nm high performance and low-power CMOS technology featuring fully-depleted tri-gate transistors, self-aligned contacts and high density MIM capacitors, 2012 IEEE Symposium on VLSI Technology (VLSIT), Digest of Technical Papers, pp. 131-132. doi: 10.1109/VLSIT.2012.6242496.

[27] T. Kent, M. Edmonds, R. Droopad, A.C. Kummel, InGaAs (110) surface cleaning using atomic hydrogen, Solid State Phenom. 219 (2015) 47–51, https://doi.org/10.4028/www.scientific.net/SSP.219.47.

[28] L. Song, D. Yang, X. Yu, Investigation on the impact of hydrogen on the passivation of silicon surface states in clean and copper contaminated conditions, AIP Adv. 9 (2019), 105102, https://doi.org/10.1063/1.5122253.

[29] Y. Wimmer, A.-M. El-Sayed, W. Gös, T. Grasser, A.L. Shluger, Role of hydrogen in volatile behaviour of defects in SiO2-based electronic devices, Proc. R. Soc. A 472 (2016) 20160009, https://doi.org/10.1098/rspa.2016.0009.

[30] L. Diez-Merino, I. Beinik, C. Teichert, P. Tejedor, Conductive atomic force microscopy study of InAs growth kinetics on vicinal GaAs (110), Appl. Phys. Lett. 95 (2009), 123103, https://doi.org/10.1063/1.3232234.

[31] M. Benedicto, P. Tejedor, Selective area growth of $In_xGa_{1-x}As$ nanowires on $HfO_2$ templates for highly scaled NMOS devices, MRS Adv. 4 (2019) 337–342, https://doi.org/10.1557adv.2019.96.

[32] M.F. Al-Kuhaili, S.M.A. Durrani, I.A. Bakhtiari, M.A. Dastageer, M.B. Mekki, Influence of hydrogen annealing on the properties of hafnium oxide thin films, Mater. Chem. Phys. 126 (2011) 515–523, https://doi.org/10.1016/j.matchemphys.2011.01.036.

[33] S. Choi, Y. An, C. Lee, J. Song, M.-C. Nguyen, Y.-C. Byun, R. Choi, P.C. McIntyre, H. Kim, Effects of $H_2$ high-pressure annealing on $HfO_2/Al_2O_3/In_{0.53}Ga_{0.47}As$ capacitors: chemical composition and electrical characteristics, Sci. Rep. 7 (2017) 9769, https://doi.org/10.1038/s41598-017-09888-6.

[34] M. Kaviani, V.V. Afanas'ev, A.L. Shluger, 2017. Interactions of hydrogen with amorphous hafnium oxide. Phys. Rev. B 95, 075117. https://doi.org/10.1103/PhysRevB.95.075117.

[35] K.G. Tschersich, V. von Bonin, Formation of an atomic hydrogen beam by a hot capillary, J. Appl. Phys. 84 (1998) 4065–4070, https://doi.org/10.1063/1.368619.

[36] B.A. Gottwald, Beam formation in molecular flow, Vak.-Tech. 22 (1973) 106–115.

[37] U. Bischler, E. Bertel, Simple source of atomic hydrogen for ultrahigh vacuum applications, J. Vac. Sci. Technol. A 11 (1993) 458–460, https://doi.org/10.1116/1.578754.

[38] E. Murad, Thermochemical properties of gaseous FeO and FeOH, J. Chem. Phys. 73 (1980) 1381–1385, https://doi.org/10.1063/1.440255.

[39] N. Jacobson, D. Myers, E. Opila, E. Copland, Interaction of wáter vapor with oxides at elevated temperatures, J. Phys. Chem. Solids 66 (2005) 471–478, https://doi.org/10.1016/j.jpcs.2004.06.044.

[40] E.J. Opila, Thermodynamics and kinetics of gaseous metal hydroxide formation from oxides relevant to power and propulsión applications, in: CALPHAD: Computer Coupling of Phase Diagrams and Thermochemistry 55, 2016, pp. 32–40, https://doi.org/10.1016/j.calphad.2016.06.007.

[41] D.L. Myers, N.S. Jacobson, C.W. Bauschlicher, Jr., E.J. Opila, Thermochemistry of volatile metal hydroxides and oxyhydroxides at elevated temperatures. J. Mater. Res. 34 (2019) 394-407. https://doi:10.1557/jmr.2018.425.

[42] E. Courcot, F. Rebillat, F. Teyssandier, C. Louchet-Pouillerie, Stability of rare earth oxides in a moist environment at high temperatures—Experimental and thermodynamic studies. Part I: The way to assess thermodynamic parameters from volatilisation rates. J. Eur. Ceram. Soc. 30(2010)1903-1909. https://doi.org/10.1016/j.jeurceramsoc.2010.02.011.

[43] X. Wang, L. Andrews, Infrared spectra and structures for group 4 dihydroxide and tetrahydroxide molecules, J. Phys. Chem. A 109 (2005) 10689–10701, https://doi.org/10.1021/jp054482i.

[44] M. García-Melchor, N. López, Homolytic products from heterolytic paths in $H_2$ dissociation on metal oxides: the example of $CeO_2$, J. Phys. Chem. C 118 (2014) 10921–10926, https://doi.org/10.1021/jp502309r.
[45] J.F. Moulder, Handbook of X-ray Photoelectron Spectroscopy: A Reference Book of Standard Spectra for Identification and Interpretation of XPS Data, Perkin-Elmer Corporation, Physical Electronics Division, Eden Prairie, MN, 1992.
[46] S. Suzera, S. Sayan, M.M. Banaszak Holl, E. Garfunkel, Z. Hussain, N.M. Hamdan, Soft x-ray photoemission studies of Hf oxidation, J. Vac. Sci. Technol. A 21 (2003) 106–109, https://doi.org/10.1116/1.1525816.
[47] M. Schie, M.P. Muller, M. Salinga, R. Waser, R.A. De Souza, Ion migration in crystalline and amorphous $HfO_X$, J. Chem. Phys. 146 (2017), 094508, https://doi.org/10.1063/1.4977453.
[48] D.S.B. Heidary, W. Qua, C.A. Randall, Evaluating the merit of ALD coating as a barrier against hydrogen degradation in capacitor components, RSC Adv. 5 (2015) 50869–50877, https://doi.org/10.1039/C5RA07264F.
[49] D. Duncan, B. Magyari-Kope, Y. Nishi, Hydrogen doping in $HfO_2$ resistance change random access memory, Appl. Phys. Lett. 108 (2016), 043501, https://doi.org/10.1063/1.4940369.
[50] K.-D. Li, J.-R. Miao, Modelling the characteristic etch morphologies along specific crystallographic orientations by anisotropic chemical etching, AIP Adv. 8 (2018), 025214, https://doi.org/10.1063/1.5021721.
[51] M.F. Al-Kuhaili, S.M.A. Durrani, I.A. Bakhtiari, M.A. Dastageer, M.B. Mekki, Influence of hydrogen annealing on the properties of hafnium oxide thin films, Mater. Chem. Phys. 126 (2011) 515–523, https://doi.org/10.1016/j.matchemphys.2011.01.036.
[52] K. Tse, J. Robertson, Defect Passivation in $HfO_2$ Gate Oxide by Fluorine, Appl. Phys. Lett. 89 (2006), 142914, https://doi.org/10.1063/1.2360190.
[53] L. Liu, H.W. Choi, J.P. Xu, P.T. Lai, Passivation of oxide traps and interface states in GaAs metal-oxide-semiconductor capacitor by LaTaON passivation layer and fluorine incorporation, Appl. Phys. Lett. 107 (2015), 213501, https://doi.org/10.1063/1.4936329.
[54] P. Tomkiewicz, A. Winkler, M. Krzywiecki, Th. Chasse, J. Szuber, Analysis of mechanism of carbon removal from GaAs(100) surface by atomic hydrogen, Appl. Surf. Sci. 254 (2008) 8035–8040, https://doi.org/10.1016/j.apsusc.2008.03.074.
[55] Y.H. Kim, J. Ree, H.K. Shin, Direct reaction of gas-phase atomic hydrogen with chemisorbed chlorine atoms on a silicon surface, J. Chem. Phys. 108 (1998) 9821, https://doi.org/10.1063/1.476457.
[56] Y. Saito, Atomic-hydrogen-induced desorption of fluorine from silicon surfaces, Appl. Surf. Sci. 81 (1994) 223–227, https://doi.org/10.1016/0169-4332(94)00153-7.
[57] H.H. Huang, Z. Zou, X. Jiang, G.Q. Xu, Photo-induced dissociation of $H_2S$ on GaAs (100), Surf. Sci. 396 (1998) 304–312, https://doi.org/10.1016/S0039-6028(97)00679-1.
[58] M. Benedicto, 2012. Selective epitaxy and lateral regrowth of GaAs and InGaAs on nanostructured HfO2/GaAs substrates: Surfactant effect of atomic hydrogen. PhD thesis. Universidad Autónoma de Madrid, Madrid, Spain. http://hdl.handle.net/10486/11669.